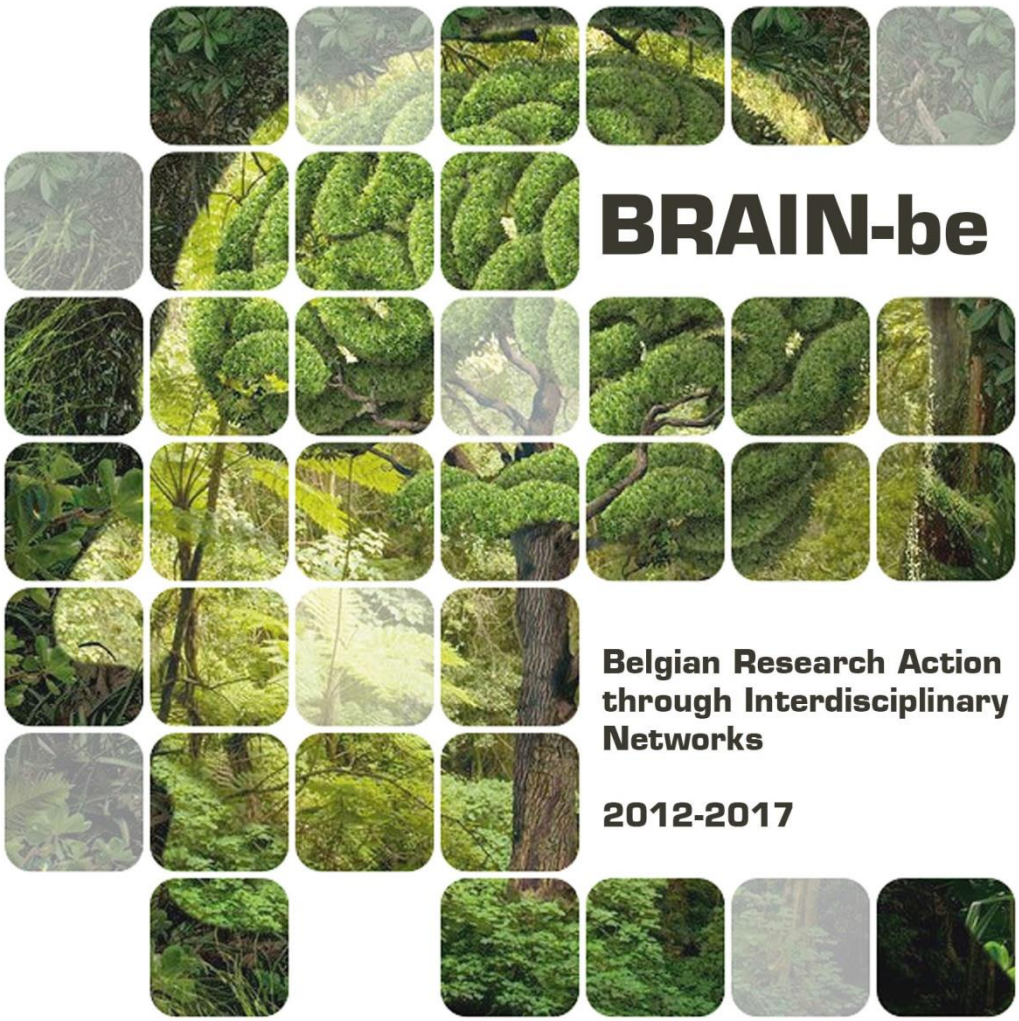

MOMA

Multi-wavelength Observations and Modelling of Aurora

H. Lamy (BIRA-IASB) – B. Hubert (LPAP) – G. Cessateur (BIRA-IASB) – M. Echim (BIRA-IASB)

Axis 2: Geosystems, universe and climate

belspo .be

NETWORK PROJECT

MOMA

Multi-wavelength Observations and Modelling of Aurora

Contract - BR/175/A2/MOMA

FINAL REPORT

PROMOTORS: H. Lamy (BIRA-IASB)
B. Hubert (LPAP)

AUTHORS: H. Lamy (BIRA-IASB)
B. Hubert (LPAP)
G. Cessateur (BIRA-IASB)
M. Echim (BIRA-IASB)

belspo .be

Published in 2022 by the Belgian Science Policy Office
WTCIII
Simon Bolivarlaan 30 Boulevard Simon Bolivar
B-1000 Brussels
Belgium
Tel: +32 (0)2 238 34 11
http://www.belspo.be
http://www.belspo.be/brain-be

Contact person: Koen Lefever
Tel: +32 (0)2 238 35 51

H. Lamy, B. Hubert, G. Cessateur, M. Echim,. ***Multi-wavelength Observations and Modelling of Aurora,*** Final Report. Brussels : Belgian Science Policy Office 2021 – 36 p. (BRAIN-be - (Belgian Research Action through Interdisciplinary Networks))

TABLE OF CONTENTS

1. INTRODUCTION

The mechanisms behind the formation of auroras in the polar regions of Earth have intrigued scientists for a long time. A large fraction of the energy flowing from the solar wind to the Earth is channeled through the Earth's magnetosphere to the polar ionosphere, where it manifests itself in the phenomenon of the aurora or "polar lights". The auroral current circuit can be viewed as being composed of four elements: (i) a generator in the equatorial magnetosphere, (ii) a load in the ionosphere that are coupled together by (ii) the upward and (iv) the downward current regions along magnetic field lines. Auroras have also been observed from all the magnetized planets in the solar system (e.g. Bhardwaj & Gladstone, 2000; Bertaux et al., 2005; Stallard et al., 2008) with different characteristics from Earth since their atmosphere and magnetosphere are different, but the fundamental plasma processes behind the formation of the aurora are universal. Therefore, studying them is a key to a better understanding of related processes in solar system and even cosmic plasmas (e.g. Hallinan et al., 2015). By studying auroral physics we also obtain a better understanding of near-Earth space, and this is for example important for our ability to protect ourselves against space weather hazards.

Auroras manifest through electromagnetic emissions at different wavelengths, which themselves offer different observational windows on the phenomenon:

- As the electrons precipitate into the upper atmosphere and ionosphere in the polar regions, they impact and excite the atmospheric atoms and molecules and create beautiful dynamical optical phenomena observable by naked eye and quantified by scientific instruments. The most intense auroral emission lines are the green (557.7 nm) and red (630.0 nm) emissions due to excited oxygen atoms O I and the blue (427.8 nm) one due to the first negative band (1NG) of N2+. These emissions are produced at altitudes between ~ 100 and 220 km. The visual aurora appear in a variety of forms such as arcs, spirals, … and on spatial scales from kilometer to thousands of kilometers. Discrete auroral arcs are intermediate scale structures and also the optical signature of electron acceleration processes in magnetospheric regions located at altitudes of several thousand kilometers. They can be quasi-static or show very rapid variations or motions (e.g. Borovsky, 1993; Frey et al., 2010). Optical observations can be done remotely from the ground using all-sky or narrow angle cameras or via imagers onboard spacecraft.
- Aurora are also observed remotely in the ultraviolet using far ultraviolet (FUV) imagers onboard satellites capturing images of the auroral oval at various wavelengths such as Lyman-a HI (121.6 nm), O I (130.4 nm and 135.6 nm) or the Lyman-Birge-Hopfield (LBH) bands of N2 (140-150 nm and 165-180 nm), produced either by electrons or protons. Indeed, both the electron and proton aurora produce secondary electrons which impact atoms and molecules of the atmospheric gas, exciting typical visible and FUV emissions. Space borne remote sensing and imaging of the Earth aurora has been a major source of scientific data in the field for decades. The POLAR and IMAGE missions carried FUV global imagers, while some of the DMSP (Defense Meteorological Satellite Program) satellites carried UV spectro-imagers similar to that of satellite TIMED (Thermosphere Ionosphere Mesosphere Energetics and Dynamics). Far ultraviolet imaging is often preferred to visible imaging because those systems are less contaminated by sunlight. Global images of the aurora allow to monitor the auroral energy input in the Earth ionosphere. In particular, the IMAGE-FUV images were used to estimate the

auroral local flux and global hemispheric power due to both the electron and proton aurora (Hubert et al., 2002). Substorm studies were a major part of the IMAGE-FUV data analysis including substorm onset location statistics (Gérard et al., 2004, Coumans et al., 2007), magnetic flux opening and closing (e.g. Hubert et al., 2006a; Milan et al., 2007), influence over the ionospheric conductance (Coumans et al., 2004), among others.

- At radio wavelengths, the most powerful radio emission from Earth is the Auroral Kilometric Radiation (AKR). These radio emissions are produced by precipitating electrons and generated nearly permanently above the auroral region (Gurnett, 1974). Most of the time the AKR cannot be detected on the ground because of the shielding by the dense ionospheric plasma but it can be observed by instruments in space. The radio spectrum of AKR peaks at about 100-400 kHz and the integrated radiated power typically can reach 10^9 W during substorm events. It is reliably established that the sources of AKR are thin cavities oriented tangentially to the auroral oval and aligned with the background magnetic field (e.g. Louarn & Le Quéau 1996a,b). An electron cyclotron maser mechanism is thought to be responsible for these emissions but how the electron distributions necessary for the generation of these waves are created remains an open question. The topic is of interest in magnetospheric physics, where it has been studied for example using the Cluster satellites (Mutel et al. 2008) but it is also potentially important to detect auroral radio emissions from exoplanets (e.g. Nichols & Milan, 2016).

2. STATE OF THE ART AND OBJECTIVES

Although auroras have been regularly observed from the ground or from space for several decades, many aspects of the auroral circuit are still poorly known. For example, what are the characteristics of the magnetospheric generator and where is it located? What are the physical mechanisms determining the structure of the large-scale field-aligned electric fields and the acceleration processes of the particles? How can we model the whole auroral circuit in a self-consistent way?

Future space missions, such as the joint ESA/CAS SMILE mission, will use FUV auroral imaging (alongside X-ray imagers) to address questions still debated: what are the fundamental mechanisms governing the dayside solar wind/magnetosphere interaction? What is the exact definition of the substorm cycle itself? How do Coronal Mass Ejections (CME) driven storms arise and what is their relationship to substorms?

Regarding the Auroral Kilometric Radiation (AKR), although the electron cyclotron maser instability is widely accepted to be the fundamental mechanism responsible for its generation, how the radiation propagates and escapes from the source is still unclear.

The partners in MOMA will combine their expertise with auroral observations and modelling to shed some light on these questions. BIRA-IASB has developed a physically-based model coupling a magnetospheric generator to an ionospheric load on one hand, and a Vlasov simulation code on the other hand, both able to describe the upward and downward auroral current regions with various degrees of sophistication. Ionospheric codes are also available either from LPAP/INASAN (Monte Carlo code) or BIRA-IASB (kinetic transport code called AeroPlanets/TRANS4). All these codes provide information on some parts of the auroral circuit. On the observational side, BIRA-IASB and LPAP have long-term expertise in analysing data from spacecraft such as Cluster or IMAGE or ground-based radar data obtained with EISCAT or SuperDARN. Recently, BIRA-IASB has acquired expertise in tomographic-like inversion of optical multi-station observations obtained with the Auroral Large Imaging System (ALIS) network, providing the unique capability of obtaining two-dimensional (2-D) fluxes of precipitating electrons along latitude/longitude.

Objectives: This project aims at improving our understanding of auroral acceleration and associated phenomena through observations at several wavelengths and models. Four topics of research are proposed:

1) To use ground-based optical observations with the ALIS network to obtain 2-D energy fluxes of precipitating electrons and use them:

- To characterize the properties (densities, temperatures and location) of the magnetospheric generator. Complementary data from spacecraft will be used whenever available.
- To produce UV emission line profiles that can be compared with remote data obtained by instruments on-board satellites.

2) To use FUV observations from IMAGE. More specifically, we will:

- Combine FUV imaging of the proton aurora from the SI12 instrument and ground-based superDARN radar data to estimate the location of the open-closed field line boundary, the

open geomagnetic flux and the reconnection voltage at the dayside magnetopause and in the magnetotail.

- Upgrade the software to allow the determination of these physical quantities using images of the electron aurora from the IMAGE-WIC and SI13 instruments. This will be a major contribution to the analysis of the data from the future SMILE mission.
- Compare the imaging of the FUV aurora with the EUV remote sensing of the plasmasphere.

3) To model the whole auroral circuit in the Earth's magnetosphere-ionosphere system in a self-consistent way by coupling an electrostatic Vlasov simulation code to an ionospheric code. This third topic is the natural theoretical complementary of the observational framework described in the preceding topics.

4) To develop an electromagnetic Vlasov simulation code that can be used to model AKR emissions.

3. METHODOLOGY

The MOMA team has combined existing expertise among the partners to achieve most of the four objectives listed above. Unfortunately, due to the unexpected departure of a collaborator at BIRA-IASB at mid-course of the project, the practical know-how about the Vlasov electrostatic code was a bit lost and as a consequence, topic 4 could not be covered as planned. Instead, important work related to the measurement of polarization of auroral lights was carried out. The methods used for all these topics are described below.

Topic 1: Analysis of ground-based optical and radar observations

1.1 : Electron precipitating fluxes from ALIS and EISCAT data

In order to retrieve the 2-D energy fluxes of the precipitating electrons, two consecutive inversions of optical observations of the blue line (427.8 nm) with the ALIS network were considered in this project. We have been using and upgrading MATLAB codes, developed in-house at BIRA-IASB. Another inversion of electron densities measured along the local geomagnetic field line by the EISCAT radar was also considered for validation of the 2-D procedure using optical data. The general method is presented in full detail in Simon Wedlund et al. (2013).

The first step consists of a 3-D reconstruction of the VER of the blue spectral line at 427.8 nm from N_2^+ 1NG(0,1) band using tomographic-like techniques and optical data from the ALIS network. The 2-D intensity of each pixel in an image obtained at each station *s* can be seen as a line integral across the 3-D distribution of the auroral intensity source. There is then a direct link between the intensities in all pixels at station *s* with the 3-D auroral volume emission rate, expressed within a transfer matrix K. We apply both the Multiplicative Algebraic Reconstruction Technique (MART) or the maximum entropy method (MEM) as inversion method to retrieve the 3-D VER.

The second step consists in an additional inversion of these blue VER using the fact that the blue band of N_2^+ is only excited by electron impact and thus depends linearly on the incoming electron precipitation flux. Indeed, the blue emission rate is proportional to the energy deposition rate (Janhunen, 2001), VER = ζ ε, with ζ the excitation efficiency expressed in ph/keV and ε the energy deposition in eV cm^{-3} s^{-1}. ζ has an altitude dependence (Partamies et al., 2004) given by

$$\zeta(z) = \frac{n_{N_2}(z)}{n_{N_2}(z) + 0.7\, n_{O_2}(z) + 0.4\, n_O(z)} \cdot 0.628.$$

Eventually, the blue VER (in units of cm^{-3} s^{-1}) can then be expressed as VER = **B** Φ, with the precipitation flux vector Φ and the matrix **B** which contains all the physics of the degradation of the electrons in the Earth's ionosphere as expressed via a forward model (Rees, 1989) :

$$B_{ij} = B(z_i, E_j)\,\Delta E_j = \frac{\zeta(z_i)\,\Lambda\left(\frac{s(z_i)}{R(E_j)}\right)\rho(z_i)\,E_j\,(1-\mathcal{A}(E))\,\Delta E_j}{R(E_j)}$$

with Λ the energy dissipation function (from Sergienko et al 1993), ρ the atmospheric mass density model (MSISE-00), and R(Ej) the electron range in air (from Barrett & Hays 1976). The flux Φ can then

be retrieved using an inversion of this equation, $\Phi = \mathbf{B}^{-1}$ VER. For this, we are using again the MART and MEM techniques with Chi-squared test for optimization.

For the EISCAT radar measurements, the method is similar to the one used for the optical measurements obtained with ALIS. First, we extract the altitude-dependent electron density n_e from the incoherent radar data. We can estimate the electron production rate q such as $q = \alpha n_e^2$, with α being the electron recombination rate from abundant O_2^+ and NO^+ species. The electron production rate q (in m^{-3} s^{-1}), in the upper atmosphere can be expressed by the matrix form $q = \mathbf{A}\,\Phi$, where **A** (in eV m^{-1}) is the energy deposition matrix which contains the physics parameters. Again, the inversion problem becomes $\Phi = \mathbf{A}^{-1}\,q$, in order to retrieve the precipitating differential electron flux at the top of the atmosphere along the local geomagnetic field line. For doing so, we use again the MART and MEM techniques.

1.2: Properties of the magnetospheric generators

In parallel, we developed a method to estimate the properties of a magnetospheric generator using a quasi-electrostatic magnetosphere-ionosphere coupling model and in situ or remote sensing observations of discrete quiet arcs. We first construct an ensemble of Vlasov equilibrium solutions for generator structures formed at magnetospheric plasma interfaces. For each generator solution, we compute the ionospheric electric potential from the current continuity equation. Thus, we estimate the field-aligned potential drop that allows us to assess several properties of the discrete auroral arc, such as the field-aligned potential difference, the field-aligned current density, the flux of precipitating energy, and the height-integrated Pedersen conductance. A minimization procedure based on comparing the numerical results with observations is defined and applied to find which solution of the current continuity equation and which generator model give auroral arc properties that best fit the observations. The procedure is validated in a case study with observations by DMSP and Cluster and can be generalized to other types of data. The main conceptual elements and the validation tests are included in Echim et al. (2019). This method is rather general and can in particular be applied to auroral experimental data collected by the ALIS network.

<u>Topic 2:</u> use proton aurora observations in combination with superDARN radar data to estimate the location of the open-closed field line boundary, the open geomagnetic flux and the reconnection voltage at the dayside magnetopause and in the magnetotail

2.1. Comparison of the reconnection rate evaluated in-situ and in the ionosphere.

In situ measurements of the properties of the reconnection site is available from observations from the ESA-Cluster mission. A restricted set of reconnection site crossings have been identified previously by other authors. However, comparing ionospheric estimates of the reconnection rate with in-situ measurements is anything but straightforward because

a. In situ measurements only provide the reconnection electric field, sometimes in an indirect manner.
b. The crossing needs to be “frank”, i.e. the spacecraft tetrahedron must cross the relatively tiny reconnection site very closely, because the properties of the magnetospheric plasma can vary over relatively small scales near the reconnection site.

c. The reconnection rate is the integral of the electric field along the reconnection line, which intersects the Cluster orbit at only one point, so that the measured electric field is representative of the reconnection site only over a restricted portion of the line.
d. Comparison with the ionospheric measurement requires finding the point of the open-closed field line boundary that maps to the Cluster location along the magnetic field line joining them, considered as a (fair) electric equipotential.
e. Near the open-closed field line boundary, the topology of the magnetic field is poorly given by (semi-)empirical magnetic field models available to the scientific community.

The following method was followed to quantitatively validate the ionospheric method and compare it to in-situ observations:

1. A crossing of the reconnection site by the Cluster spacecraft tetrahedron is selected in the literature, making sure it closely crosses the reconnection line by comparing the observation of the different spacecraft along their track.
2. The Tsiganenko field line model is used to map the location of the spacecraft down to ionospheric altitude. As such model cannot rigorously represent the field in that region, the ionospheric foot-point if found somewhat away from the polar boundary of the aurora, used as a proxy for the open-closed field line boundary (OCB), so that only the MLT of the foot-point is retained, denoted MLT^*.
3. An MLT interval bracketing MLT^* is determined over which the reconnection electric field does not much vary along the polar cap boundary.
4. The MLT interval bounds, determined at ionospheric altitude, are mapped back to the ionosphere along the magnetic field line, as close as possible to the Cluster location. The distance separating these field lines near the Cluster tetrahedron (L_y) is retained as the length of the reconnection line corresponding to the selected ionospheric MLT sector bracketing MLT^*. Exact mapping is not needed here, as only the appropriate length is required to compute the reconnection voltage, and magnetic field lines are mostly parallel to each other far away from the planet.
5. The in-situ reconnection rate is evaluated at the reconnection site by multiplying the transverse (y) component of the electric field by the length (L_y) determined above at step 4. This value is compared with the voltage computed as the line integral of the ionospheric reconnection electric field.

In addition to this direct comparison of the reconnection rate, the energy input into the nightside reconnection site can be estimated as the Poynting flux integrated along a surface delineated by the the tail field lines between the reconnection site and the plasmapause (i.e. at some 5 Re altitude) and mapping to the above-defined MLT sector where the electric field is expected to remain fairly constant. This energy input can then be compared with the auroral energy input of the precipitating particles. The Poynting flux needed for the magnetospheric computation is $\left|\vec{E} \times \vec{B}\right|/\mu_0$, which, under the assumption of a perfectly conducting material can be estimated as $U_{in}\, B^2/\mu_0$ where E is the electric field, B the magnetic field, μ_0 is the magnetic permittivity of empty space, and U_{in} is the velocity of the plasma flowing in the reconnection site (i.e. crossing the surface defined above). The plasma velocity and the magnetic field are measures in-situ by the Cluster spacecraft.

2.2 Magnetic reconnection and ionospheric signatures during major storms.

In this work, observations of the Earth plasmasphere is compared with ionospheric estimates of the reconnection rate and open magnetic flux. The plasmasphere, observed with the IMAGE-EUV instrument, has its boundary, the plasmapause, mostly governed by the balance between the convection electric field and the corotation electric field. This view is however strictly valid at steady state only, which is rarely perfectly reached. A first study was undertaken to identify plasmaspheric signatures of substorms, considering that modifications of the convection electric field that occurs during substorms may have impacted the location of the plasmapause. This study revealed inconclusive, and further efforts were therefore dedicated to the study of geomagnetic storms, which occur at a planetary scale and are known to significantly disturb the radiation belts and plasmasphere. The IMAGE-EUV images are therefore used to identify the plasmapause as the region of space where the plasmaspheric density abruptly drops, signalizing the transition between trapped (cold) particles orbit to “free” particle orbits subject to magnetospheric convection.

The Hepner-Maynard boundary delineates the ionospheric region around the magnetic pole where plasma motion is governed by magnetospheric convection. It can be expected that this boundary, of which the location can be estimated from the SuperDARN observation, will be related to the evolution of the trapped population at storm times.

Topic 3: The auroral current circuit

3.1. Return flux of particles from the aurora towards the magnetosphere.

The Monte-Carlo model previously developed by our Russian colleagues of the Institute of Astronomy of the Russian Academy of Sciences in Moscow was deeply upgraded in order to allow for a detailed modelling of the upward and downward flux of auroral particles. This includes the introduction of variance reduction techniques allowing for a faster stochastic accumulation of the distribution function of the particles energy and direction of motion. This is equivalent to studying the velocity distribution function in polar coordinates and substituting the velocity modulus to the kinetic energy. The simulation code was adapted in order to allow for an energy and angular binning of the particles precipitating into the upper layer of the modelled atmosphere and then retrieving the properties of the return flux of electrons moving upward and leaving the atmosphere. The model can also be used to compute the excitation rate of different auroral emissions, but this ability was not used for the sake of the current project. A server-class computer was bought for massively running the code and obtain the results. Indeed, not only was that new machine used for the computation, but also three other, older servers, previously bought with funding from both BELSPO and FNRS. The availability of these machines made it possible to enhance the number of energy and angular bins of the input flux simulated at the top of the model. A software was written that schedules and manages the tasks executed by the different servers. It writes the input files needed for the Monte-Carlo code, copies them to the server that has computational headroom and watch for the retrieval of the Monte-Carlo output. Each time a Monte-Carlo simulation ends, the scheduling software launches a new run on the server that just ended that simulation, until all the runs requested by the user have been completed. Such a strategy is necessary for the massive production of Monte-Carlo results. Using all these servers, a full set of runs, as we defined it, can take more than a week, with a total number of available, computing units amounting to 112 CPU threads shared among the several servers (a part of the

resources was left free for other users). We note here that the new server was also used for the analysis of the IMAGE mission data (see above). We installed the IMAGE database and software on the new server and solved compatibility issues between the mission software and recent Linux operating systems, which allows us using them on more performant and more recent computers (which ensures we keep easy access to the data, even if, in the future, our older server ultimately fails and must be dismantled).

3.2 Electrostatic Vlasov simulation code

An electrostatic Vlasov simulation code developed at BIRA-IASB in the recent years (Gunell et al., 2013) was used. This code is 1D in configuration space and 2-D in velocity space. The spatial dimension is the coordinate along the magnetic field, and the velocity dimensions are represented by the velocity parallel to the magnetic field and the magnetic moment. A stationary magnetic field is prescribed. The forces included in this model come from the magnetic mirror field, the parallel electric field, and possibly the gravitational field. The code solves a system constituted by the Vlasov equation and a Poisson type equation adapted to the magnetic field geometry. The charge per unit length of the flux tube in Poisson's equation is found by integrating the distribution functions over velocity space for all species. In the same equation, an artificial relative dielectric constant is introduced to reduce the computational effort.

3.3 : Coupling of the Vlasov code and an ionospheric model:

So far, the upward and downward current regions of the auroral circuit were simulated using this electrostatic Vlasov code, but always separately. However, these circuit elements are affected by the other parts of the circuit. The current in the downward current region is controlled by the temperature and density of the ionosphere. For upward currents, the altitude of the acceleration region is influenced by the density of the ionosphere. The ionospheric conditions are, in turn, affected by particle precipitation. The goal was to build a self-consistent model of the auroral current circuit by coupling the Vlasov simulation code to the MC ionospheric model provided by LPAP. The coupling will be realized by iterating between the models until a stationary state is reached. In this way we will be able to study both the interaction between each of the upward and downward current regions and the ionosphere and the behaviour of the complete circuit, which is essential for the understanding of the temporal development of the current and of the auroral emissions. Once this circuit model is established we will be able to simulate the response of the circuit to changes in the generator that is driving it.

Measurement of auroral polarization

In the last two decades, there was a renewed interest to know whether the auroral emissions are polarized or not, and if they are, how this would help better understand and model the upper atmosphere and improve space weather forecasting. This work was mostly led by IPAG (Institut de Planétologie et d'Astrophysique de Grenoble) with an active participation from BIRA-IASB. Several instruments were developed over the years with increasing complexity and sensitivity. The initial observations focused mostly on the red emission line at 630.0 nm because it was predicted to be polarized by impact with collimated magnetospheric electrons precipitating along the magnetic field lines (Bommier et al. 2011). The polarization is due to an imbalance between the populations of the (unresolved) Zeeman sublevels of the upper level of the transition and is parallel to the direction of

incoming electrons, so mostly parallel to the magnetic field. The polarization of the red line was confirmed by observations obtained during several campaigns in Northern Scandinavia using a spectro-photopolarimeter. The degree of linear polarization (DoLP) was measured at a few percent (~5% in average), much lower than the predicted theoretical value (~17%), most likely because the red line has many production mechanisms (including chemistry or impact with secondary electrons) which are more isotropic and therefore dilute the measured polarization. The angle of linear polarization (AoLP) also very often departs from the direction of the magnetic field. Although the red line emitted at ~220 km very often is weak (except during intense activity associated with geomagnetic (sub-)storms) and therefore produces noisy measurements of DoLP difficult to interpret, no attention was paid for a long time to the much brighter green line at 557.7 nm as it was predicted to be unpolarized since the upper level of the transition has a total kinetic moment J=0 and therefore no Zeeman sublevels. Nevertheless, recent observations (Bosse et al. 2020, 2021a) with improved versions of the spectro-photo polarimeters (called “Petit Cru” and “Grand Cru”) show that the green line is also polarized at a level of a few percent, raising again the question of the origin of the polarization. Observations of the N2+ 1st negative band emissions at 427.8 nm (blue line) and 391.4 nm (purple line) were also carried out with similar conclusions. To interpret these puzzling observations, a sophisticated polarized radiative transfer model (called POMEROL) was developed by Bosse et al. (2021b) including light pollution from nearby sources, Rayleigh scattering in the atmosphere, Mie scattering by aerosols and reflections on snow. This allows to conclude that contributions from polluting sources of light (e.g. from the village nearby in Northern Scandinavia) must be taken into account but cannot explain the complex variations of the observed DoLP / AoLP of the green, blue and purple lines and that they are related to changes in the E region (measured by other means such as observations with the EISCAT radar or magnetometers on the ground) such as ionospheric currents (both field-aligned and horizontal Pedersen/Hall currents).

4. SCIENTIFIC RESULTS AND RECOMMENDATIONS

4.1 Tomography of ground-based optical observations to obtain 2D fluxes of precipitating electrons

As an example below, we considered an auroral arc event occurring 7 March 2008 starting around 20H32 UT. Figure 1 shows the keogram of this event at 4 observations sites : Skibton, Abisko, Tjautjas and Silkkimuotka, all located in Sweden. A keogram is a time-versus-latitude plot created from the individual images captured during the night.

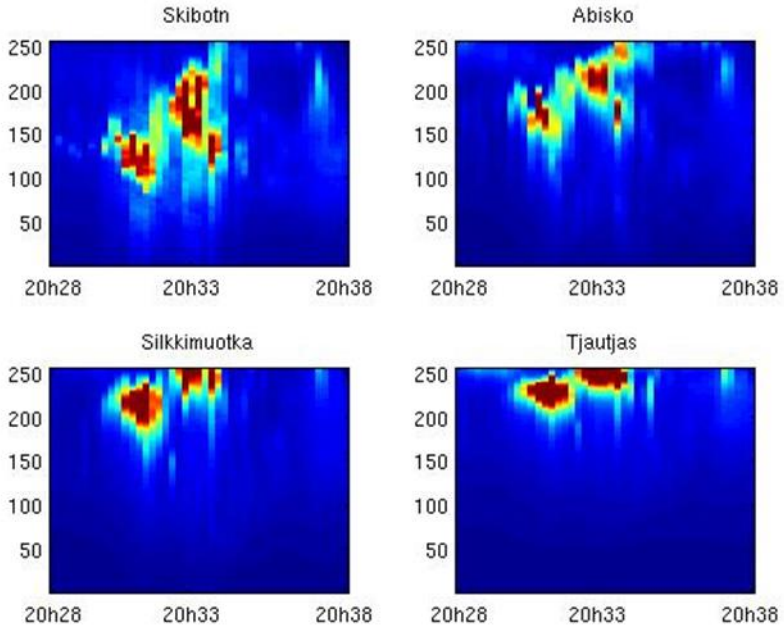

Figure 1: Keogram for the 4 observations sites presenting the auroral event occurring on March 7th, 2008 around 20H32UT. Latitude is given in pixel numbers.

From these observations, the Volume Emission Rate (VER) for the blue line emissions from the N_2^+ band at 427.8 nm can be retrieved. For doing so, we are using the tomographic-like code developed at BIRA-IASB as previously described. An example of such VER reconstruction is shown in Figure 2.

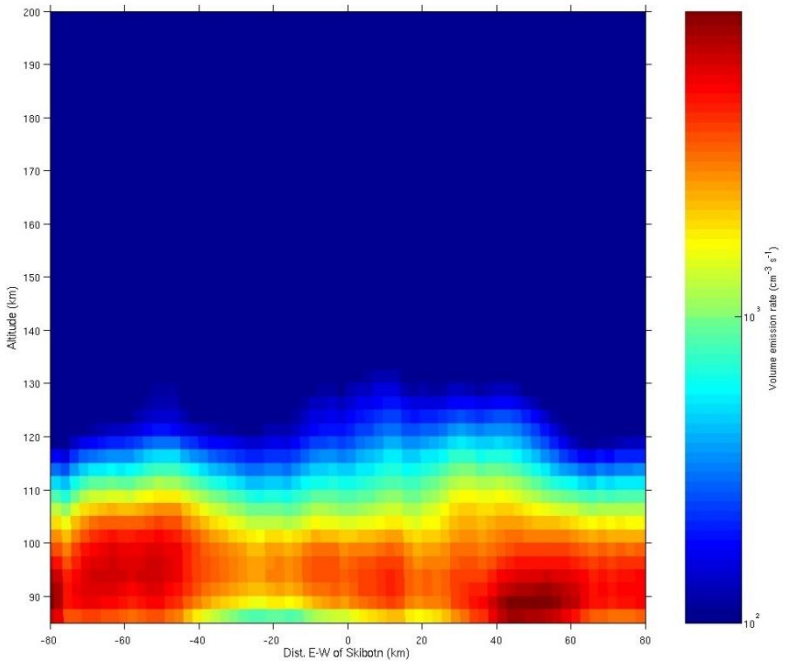

Figure 2: Vertical profile of the Volume Emission Rate (VER) for the blue line along the E-W direction centered on Skibotn.

The VER from the blue line is particularly interesting because it is directly proportional to the energy deposition rate. Simply put, VER is equal to B × Φ, where Φ is the electron precipitation flux and B is the matrix containing all the information of the energy degradation within the Earth's ionosphere. Using a second Matlab inversion code developed also at BIRA-IASB, we can obtain 2D-electron differential energy flux maps. Figure 3 presents an example of such a reconstruction, with the differential energy flux at 260 km above the EISCAT radar station, for 3 different timestamps for March 7, 2008. The electron fluxes can also be derived from the EISCAT UHF radar data, using some inversion codes based on the ionization rates mainly from O_2^+ and NO^+.

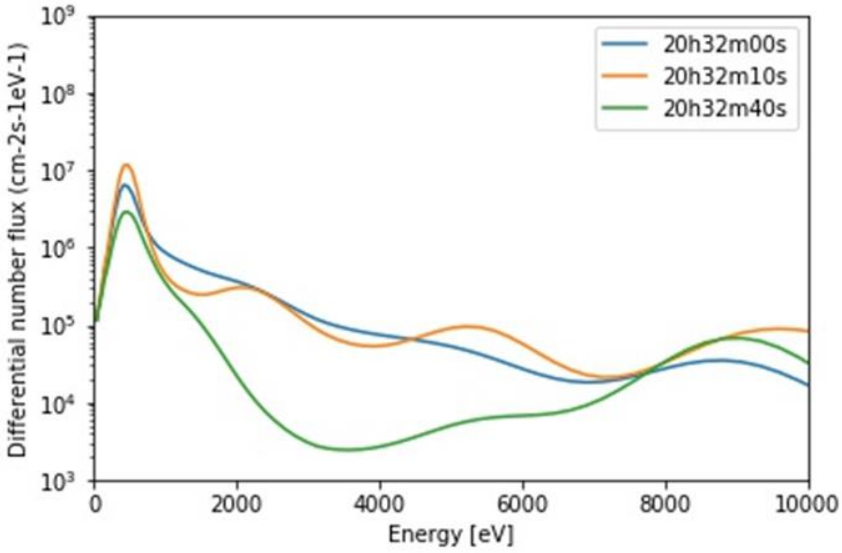

Figure 3: Electron precipitation fluxes above the EISCAT station at the top of the atmosphere (260 km altitude), for several timestamps for the auroral event occurring on March 7th, 2008.

The reconstructed precipitating electron flux from ALIS and EISCAT are then used as primary inputs to airglow models such as Aeroplanets, a particle transport model developed for studying the ionization and dissociation in the upper atmosphere of planetary bodies. The VER for the blue line emission can be calculated, and compared directly to the VER derived from ALIS observations. Figure 4 shows such comparisons for 20h32m10s, where the agreement with ALIS observations is rather good at low altitudes, there is still a discrepancy with a ratio about 1.5 at the maximum of the peak. It starts to diverge for altitudes above 140 km, but it is expected since the inversion methods are not reliable for higher altitudes. We assume a 20% uncertainty for the Aeroplanets outputs. Such comparisons have been performed also for the different timestamps discussed within figure 2.

Using the EISCAT inversion as primary input to the Aeroplanets model, we can also retrieve the blue VER for the same date. The maximum is in good agreement with ALIS observations, with a ratio of about 0.9, while there is a significant deviation at higher altitudes.

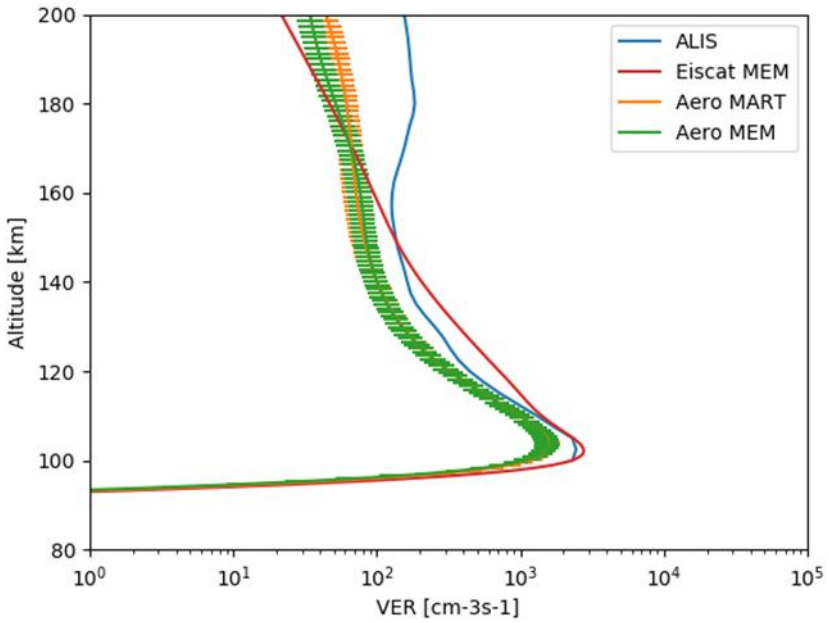

Figure 4: Blue VER obtained from Alis Observations (in blue), and Aeroplanets modelling using EISCAT (in red) and ALIS inversion (in green and orange) for 20h32m10s above EISCAT.

From the precipitating electrons flux as described from figure 3, the net energy flux (i.e. the integral over the electrons energy) can be retrieved, and we obtain 2D maps of the net energy flux at 260 km altitude as showed by Figure 5 for the auroral event at 20h32m00s. Those 2D maps are crucial parameters to retrieve the properties of the magnetospheric generator.

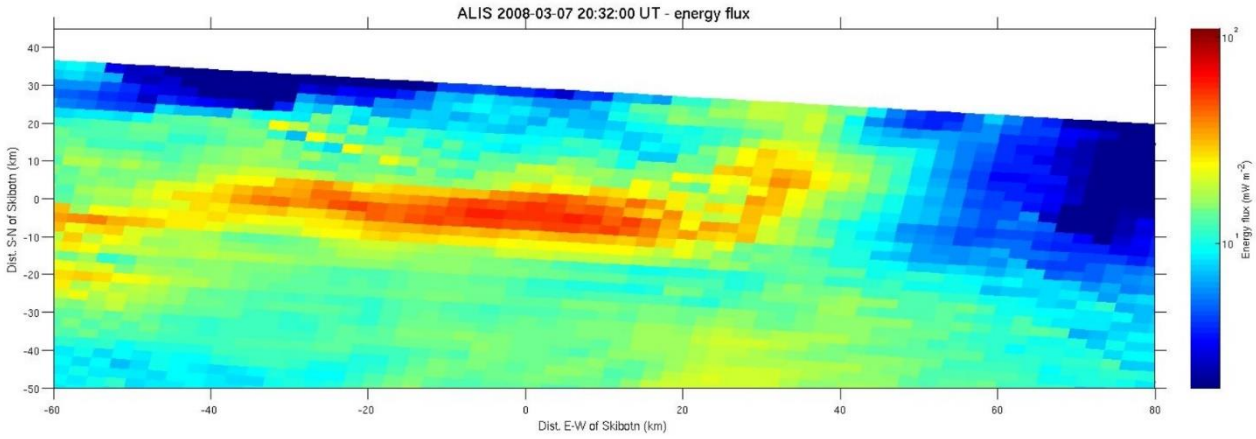

Figure 5: Net energy flux at 260 km altitude for the 20h32m00s event

From the Blue VER, it is possible to retrieve the VER for others auroral spectral lines, such as for the green line at 557.7 nm, coming from the deactivation of the atomic oxygen around 110 km altitude, but also for the red line at 630 nm also from the deactivation for the atomic oxygen but coming from 200 km altitude. Janhunen et al. (2001) proposes some intensity ratio profiles I(red)/I(blue) and I(green)/I(blue), as depicted within Figure 6, using the blue VER from Alis as reference.

The Aeroplanets model can also produce the VER for the red and green auroral spectral lines. However, the intensity ratio profiles are quite different from Janhunen et al. (2001) as showed also by Figure 5. We do provide from Aeroplanets some new expressions, fitted over the results from Figure 5, such as:

$$I_{630}/I_{427} = 10^{4-1.3\times10^{-2}(300-h)-7.7\times10^{-4}(300-h)^2+8\times10^{-6}(300-h)^3-2.5\times10^{-8}(300-h)^4}$$

$$I_{557}/I_{427} = 10^{1.16+1.25\times10^{-2}(243-h)+1.4\times10^{-4}(243-h)^2-1.5\times10^{-6}(243-h)^3-5\times10^{-8}(243-h)^4+8\times10^{-10}(243-h)^5-3\times10^{-12}(243-h)^6}$$

with *h* being the altitude in km. The values of 300 and 243 km corresponds to the altitude maximum of the ratio for Red over Blue and Green over blue, respectively.

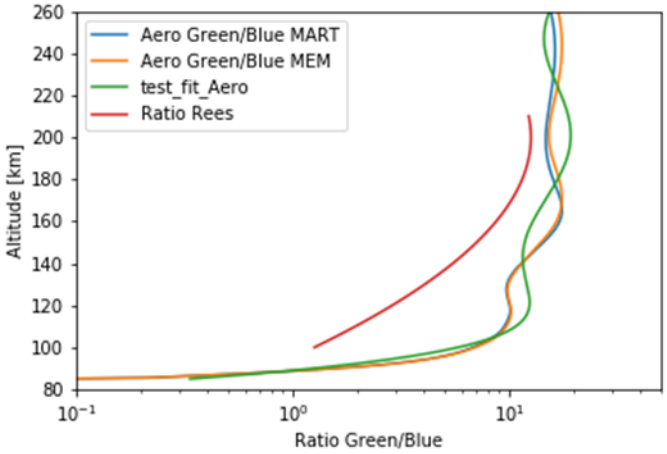

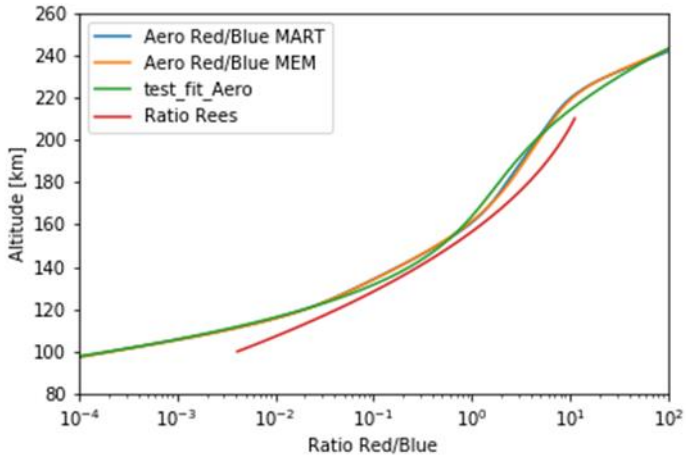

Figure 6: Ratio Green over Blue (Upper graph) and Red over Blue (Lower graph) for the Aeroplanet reconstructions (Blue and Orange), along with the fit (in green), as well as the ratio from Janhunen et al. (2001) in red.

The VER for the green spectral lines can also be retrieved from the visible ALIS observation using the tomographic inversion MATLAB code. Such reconstruction is shown within Figure 6 for the 20h32m05s event, along with the Aeroplanets green reconstruction. There is an important discrepancy between the two reconstructions. While the maximum of the profile occurs roughly at the same altitude, there is a ratio of about 70 between the two reconstructions. We consider increasing the atomic oxygen density to fix this issue. Multiplying by 2 does not solve this issue, and the medium starts to be collisional for higher density, drastically reducing the green VER. So far, we did not solve that issue, which leaves us with using the fit from Figure 6.

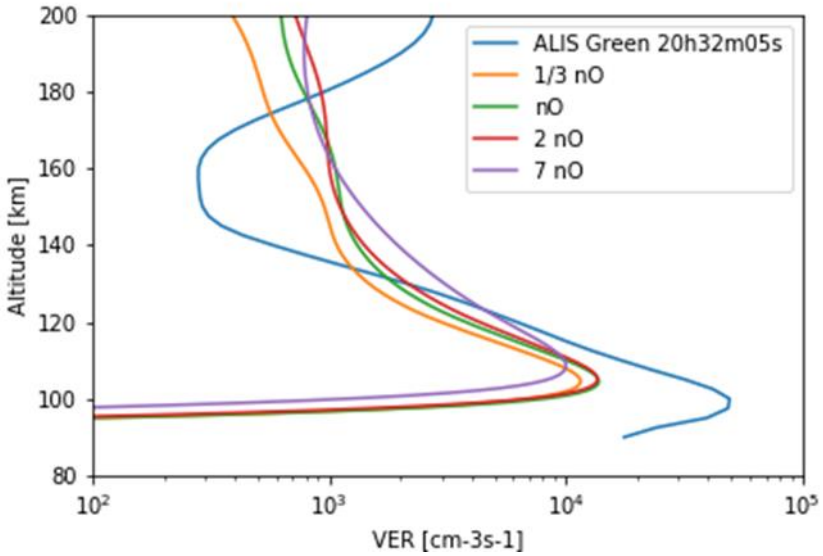

Figure 7: Green VER from Aeroplanets using differents atomic oxygen density and electrons flux at 20h32m00s compared with the Green VER from ALIS observations (in blue)

4.2 : An iterative method to estimate the properties of the magnetospheric generator from observations of the coupled quiet auroral arc

These activities were meant to fully exploit the methodology published in Echim et al (2019) and apply it on auroral experimental data collected by ALIS network during campaigns coordinated by BIRA-IASB. The aim is the to estimate the magnetospheric interface generators (MIG) properties of the arcs observed with ALIS.

The set of input parameters for the Vlasov equilibrium solution is quite large and includes:

- T_{e1}, T_{p1}, T_{e2}, T_{p1}, $T_{e\_trapped}$, $T_{p\_trapped}$, $T_{O\_trapped}$ - the temperatures of left, right and trapped populations;
- n_{e1}, n_{p1}, n_{e2}, n_{p1}, $n_{e\_trapped}$, $n_{p\_trapped}$, $n_{O\_trapped}$ - the densities of left, right and trapped populations;
- $\boldsymbol{V}_{e1}$, $\boldsymbol{V}_{p1}$, $\boldsymbol{V}_{e2}$, $\boldsymbol{V}_{p1}$, $\boldsymbol{V}_{e\_trapped}$, $\boldsymbol{V}_{p\_trapped}$, $\boldsymbol{V}_{O\_trapped}$ - the bulk velocities of left, right and trapped populations;
- $\mathbf{B}_0$ - the magnetic field in the center of the transition;
- The velocity distribution function parameters assumed for all species considered in the model (see Roth et al., 1996);
- $\Phi_1=\Phi(x_1)$and $\delta\Phi=\Phi(x_1)- \Phi(x_2)$ - the value of the electric potential at the left side and the potential difference across the interface.

The Vlasov equilibrium solution provides the profile across the interface of the electron and ion density, $n_e(x_m)$, $n_p(x_m)$, temperature, $T_e(x_m)$, $T_p(x_m)$, bulk velocity, $\boldsymbol{V}_e(x_m)$, $\boldsymbol{V}_p(x_m)$, current density, $\boldsymbol{J}_e(x_m)$, $\boldsymbol{J}_p(x_m)$, as well as of the electric potential, $\phi_m(x_m)$ and magnetic field $\boldsymbol{B}(x_m)$. In order to expand the range of possible solutions we performed additional simulations of the Vlasov model that now includes 29 instances of magnetospheric interface generator (MIG) solutions. As shown in Table 1, a parametric model of a MIG adapted for the interface between the Plasma Sheet Boundary Layer (PSBL) and the magnetotail lobe is built from a reduced set of variable parameters at the right side of the interface. This set includes: (a) n_{e2} - the electron density at the PSBL side; (b) T_{e2} - the electron temperature at the PSBL side; (c) $\boldsymbol{B}_0$ - the magnetic field in the center of the transition.

	M1	M2	M3	M4	M5	M6	M7	M8	M9	M10	M11	M12	M13	M14	M15	M16	M17	M18	M19	M20	M21	M22	M23	M21	M22	M23	M24	M25	M26	M27	M28	M26
N_{e2} [cm^{-3}]	0.31	0.62	0.9	0.2	0.15	0.31	0.31	0.31	0.31	0.31	0.31	0.31	0.31	0.31	0.31	0.31	0.31	0.31	0.31	0.31	0.31	0.31	0.31	0.31	0.31	0.31	0.31	0.31	0.31	0.31	0.31	0.31
T_{e2} [eV]	200	200	200	200	200	100	500	1000	5000	6000	7000	8000	4000	3000	2000	5000	5000	5000	4000	4000	3000	3000	2000	1000	500	2000	1000	500	200	200	200	200
B [nT]	480	480	480	480	480	480	480	480	480	480	480	480	480	480	480	460	440	420	420	400	400	380	360	360	360	360	360	360	360	345	697	256

Table 1. Twenty nine MIG model runs, denoted from M1 to M29, obtained for different sets of boundary conditions. From top to bottom, we specify the electron density, temperature and the magnetic field intensity at the "right" or PSBL- side (indexed with "2") of a plasma interface, respectively. For each set we found a Vlasov equilibrium that describes the transition between the two asymptotic states, Lobe and PSBL.

This set of parameters controls the spatial scale of the interface (through T_{e2} and $\boldsymbol{B}_0$), the value of the total particle and current density (through n_{e2}), the profile of the electric and magnetic field. All the other interface parameters take constant values as described below. We also assume that the asymptotic plasma state at the left side of the transition is compatible with magnetospheric lobe

properties and is described by fixed values of the electron and ion density (0.12 cm^{-3}), the electron and ion temperature, T_{e1}=75 eV and T_{p1}=250 eV, and the plasma bulk velocity, $\boldsymbol{V}_{ey1}=\boldsymbol{V}_{py1}$=0.5 km/s. These parameters are compatible with values reported in the literature. At the PSBL side all the other parameters are fixed: the ion temperature T_{p2}=4 keV, the plasma bulk velocity $\boldsymbol{V}_2$=8.5 km/s, compatible with observations of the PSBL. The drift velocities at the PSBL side of the interface are consistent with observations by Vaivads et al (2003) of a lobe/PSBL interface; at the lobe side we considered the drifts estimated by Echim et al (2009).

The methodology is described in detail in Echim et al (2019). We just recall here that we aim to minimize a function that includes both model parameters and observational variables. The minimization procedure is defined based on which model fits best the observations as described mathematically by the function SNORM defined below:

$$S_{\mathrm{NORM}} = \sum_{(\Pi)} S_{\mathrm{NORM}}^{(\Pi)}$$

where the summation is over the number of Π variables observed experimentally and

$$S_{\mathrm{NORM}}^{(\Pi)} = \sum_{i=1}^{N} \frac{\sqrt{\left|\left(\Pi_i{}^{\mathrm{model}}\right)^2 - \left(\Pi_i{}^{\mathrm{obs}}\right)^2\right|}}{\left|\Pi_i{}^{\mathrm{obs}}\right|}$$

is computed as a sum over all N samples available for the observable Π and from the model. The method was tested and validated with one set of observations, namely the accelerating electric potential observed by DMPS for a conjunction DMSP-Cluster (see, Echim et al., 2019). We have applied the method on another ensemble of observations, namely the flux of precipitating energy derived from a tomographic analysis of ALIS auroral observations. We used data from ALIS observations recorded on 05/03/2008 and their tomographic reconstruction, as shown in Figure 8.

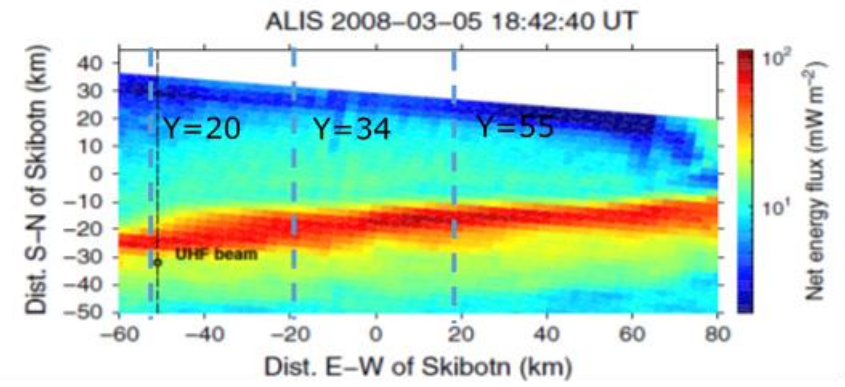

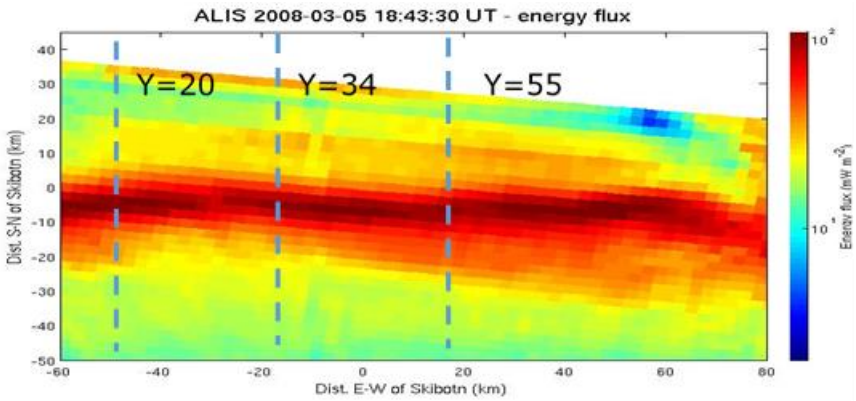

Figure 8. 2-D map of the integrated net energy flux (in mW/m2) at 18:42:40 UT (top) and 18:43:30 UT (bottom) on 05/03/2008 derived from reconstructed fluxes of precipitating electrons at 260 km altitude, determined from a tomographic analysis of ALIS data (Simon-Wedlund et al., 2013). With dashed blue lines are illustrated the cross profiles used to estimate the local properties of MIG for all models included in Table 1.

Each solution in the MIG set is constructed from the parameters summarized in Table 1 and was used to build an auroral arc model set (set_ARC) based on the principles of the magnetosphere-ionosphere coupling model developed at BIRA-IASB (Echim et al., 2007, 2008). The results are shown in Figure 9 that illustrates the main electrodynamic parameters of the arcs:

- the distribution of the energy of precipitating electrons (assumed to be Maxwellian at injection),
- the accelerating electric potential,
- the field aligned current-density,
- the flux of precipitating energy.

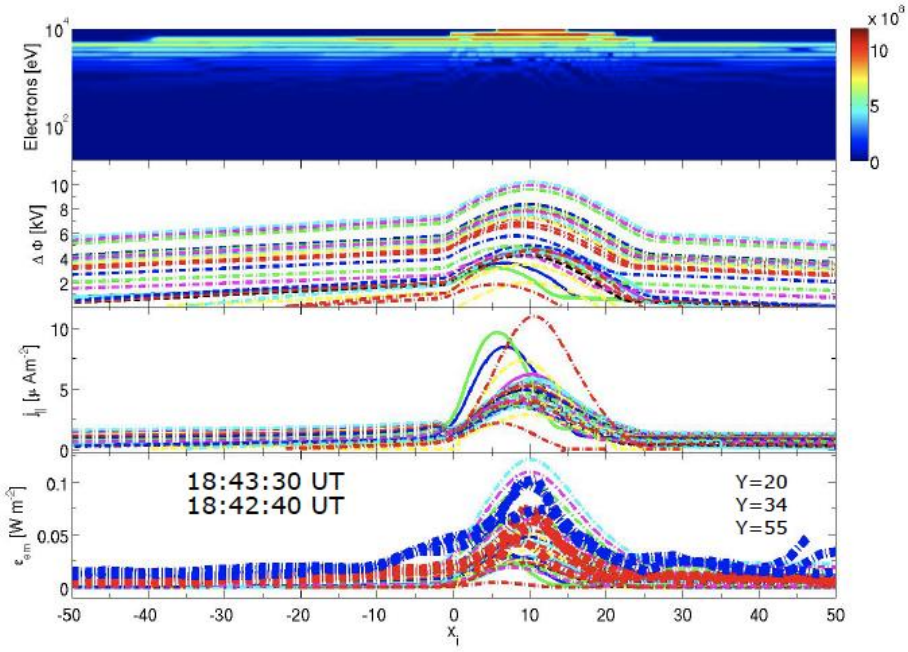

Figure 9. Set of 29 arc solutions. Panels show: energy spectrum of precipitating electrons injected at generator altitude, accelerating potential, field-aligned current density, flux of precipitating energy. Six profiles of ε_{em} from ALIS observations at 18:42:40 UT and 18:43:30 UT are superimposed in bold red and blue.

The experimental data set available from the auroral observations with the ALIS network is the flux of precipitating energy, which is then the experimental reference used to compute $S_{\text{NORM}}^{(\varepsilon_{em})}$ as described above. In Figure 9, bottom panel, we also illustrate 6 profiles of the flux of precipitating energy determined from ALIS tomographic data as a function of the distance across the arc, along the cross sections indicated in Figure 5 (parameter Y). Thus, for each of these six experimental profiles and for all 29 arc solutions we compute the value $S_{\text{NORM}}^{(\varepsilon_{em})}$.

The results of the minimization procedure for each model in set_ARC and each profile of ε_{em} are shown in Figure 10. One panel is associated for $S_{\text{NORM}}^{(\varepsilon_{em})}$values obtained for the ε_{em} profile corresponding to that respective Y value (see also Figure 8). These results show that a minimum value of $S_{\text{NORM}}^{(\varepsilon_{em})}$ is obtained for a given arc model. Indeed, at 18:42:40 UT we obtain the following estimations for the generator properties as a function of Y: for Y=20 best fit is given by model M23, for Y=34 best fit is given by model M24, for Y=55 best fit is given by model M23. These results seem to indicate the properties of the generator are quite stable in the azimuthal direction. Also, at 18:43:30 UT we obtain the following solutions: for Y=20 best fit is given by model M20, for Y=34 best fit is given by a double solution, models M18 and M20, the same situation for Y=55.

The fact that the arc model that best fit observations changes with Y and/or with time can indicate local and/or time variations of the generator properties (under the assumption the arc is quasi-stationary and the acceleration is quasi-static). Further work is needed to better understand the significance of these results for the magnetosphere – ionosphere coupling, which is precisely the work planned for the next phase of the project.

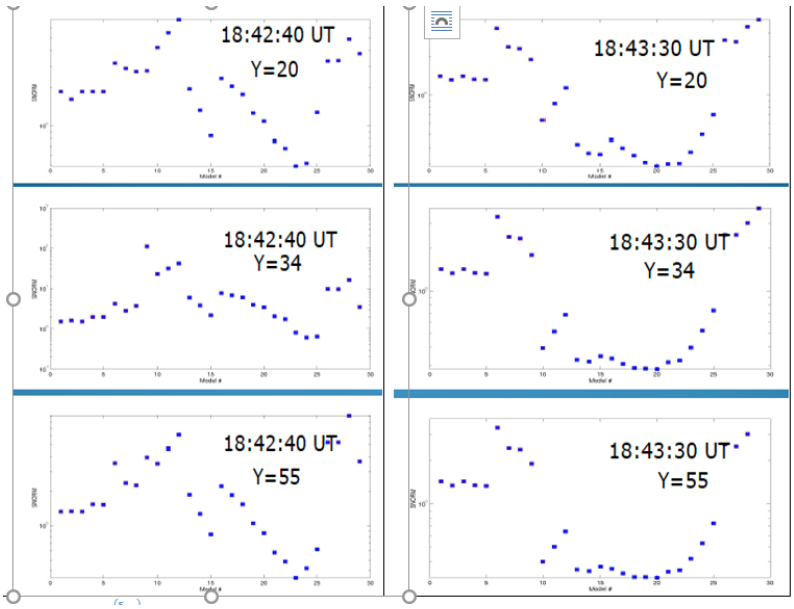

Figure 10. $S_{\text{NORM}}^{(\varepsilon_{em})}$values for the 29 arc solutions selected in *set_ARC* and depicted in Figure 6. The experimental reference observable is the flux of precipitating energy estimated from a reconstruction based on a tomographic analysis of ALIS data shown in Figure 5. Each panel correspond to a ε_{em} profile in the direction normal to the arc, obtained for that specific location (specified by the value Y, and indicated also in Figure 8).

4.3. Return flux of particles from the aurora towards the magnetosphere.

Figure 11 shows an example of the upward energy flux computed at the top of the auroral atmosphere. The average energy of the precipitating energy is assumed to be 10 keV, and the input energy flux is normalized to 1 mw m^{-2}. The model computes the electron differential energy flux in all pitch angle bins with a resolution of 10 degrees. The energy resolution is 1 eV. The flux, despite a smoothing applied to the results that degrades the energy resolution to ~30 eV, shows stochastic variations inherent to the Monte-Carlo method. A significant upward flux is found at 10 keV. This is understandable, as some of the precipitating particles will encounter elastic collisions scattering their velocity vector close to the horizontal direction, or even in the upward direction. If such scattering occurs above the altitude range of intense collisional regime, those particles will reach their mirror point or directly move upward, a fraction of which travelling freely up to the top of the atmosphere. The energy flux carried by particles having a lower energy is relatively weaker.

The effect of the initial pitch angle range is seen by comparing panels a and b. When the initial pitch angle is closer to the horizontal direction, the probability of such particle of mirroring (or being scattered upward) before having lost a large fraction of its energy becomes larger. Consequently, the upward return flux becomes relatively larger in the high energy range.

The total return flux at the top of the atmosphere was found to be on the order of a few percent of the input energy flux. This flux will contribute to the upward particle flux in the auroral acceleration region. A very detailed modelling will therefore take advantage of including the return flux, introducing a bidirectional coupling between the ionosphere and the near-Earth magnetosphere.

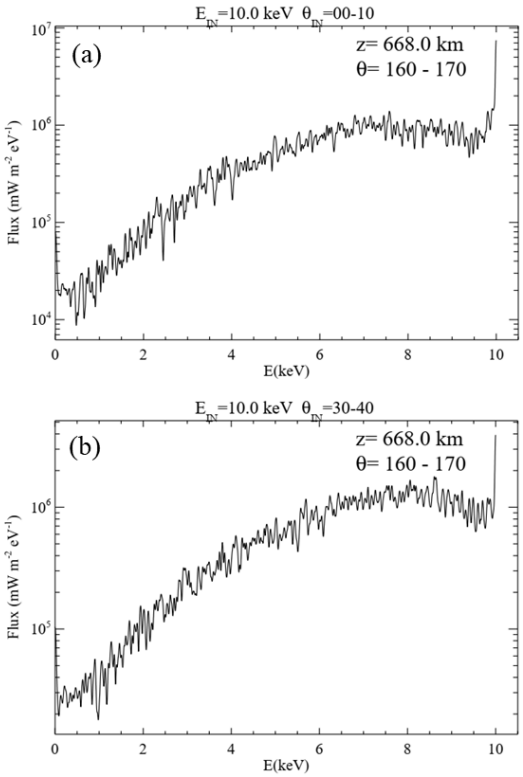

Figure 11. Upward energy flux modelled at the top of the auroral atmosphere, of particles having a pitch angle ranging between 160 and 170 Deg (from nadir). The input electron flux is 1 mw/m2, the precipitating particles have an energy of 10 keV and their pitch angle is distributed in the range 0 – 10 Deg (a) and 30- 40 Deg (b).

4.4. Comparison of the reconnection rate evaluated in-situ and in the ionosphere.

Several cases of Cluster crossing the reconnection site were analysed. A nearly perfect match was found between the reconnection voltage estimated in situ and that derived at ionospheric altitude, as shown in the figures below. Very close crossing of the night-side reconnection site occurred on 22 August and 15 September 2001. The magnetic field mapping between the ionosphere and the Cluster location allowed to retrieve the length L_Y needed to compute the in-situ voltage (Figure 12). As explained above, the mapped field lines are all nearly parallel to each other, so that exact mapping back to the Cluster location is not required for the sake of determining L_Y.

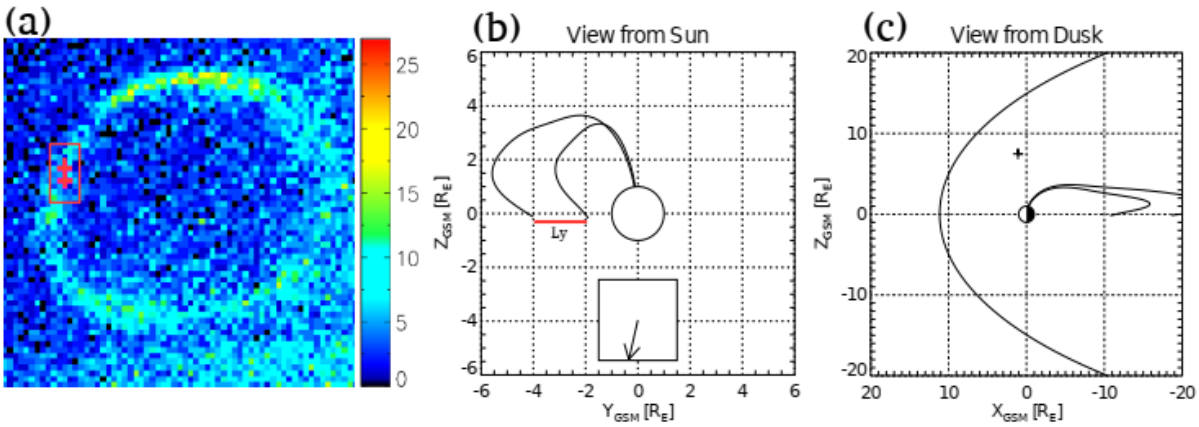

Figure 12. Mapping of two magnetic field lines from the polar ionosphere to the Cluster's location on the night-side on 22 August 2001 at 09:41 UT imaged using IMAGE FUV-SI12. The mapping is realized using the Tsyganenko-96 model. The red crosses in panel (*a*) indicate the ionospheric foot-points of both mapped field lines. Panel (*b*) shows the mapping to the tail along the y and z axis from which we deduce L*y*. Panel (*c*) is a view of the mapping from Dusk, and it shows the field lines mapping to the tail where the Cluster spacecraft is located. The black cross shows the location of IMAGE.

Figure 13 shows the reconnection voltage obtained in-situ and at ionospheric altitude during the Cluster crossing of the night-side reconnection region on 22 August and 15 September 2001. Although uncertainties are hard to estimate for both methods, it clearly appears that they closely agree.

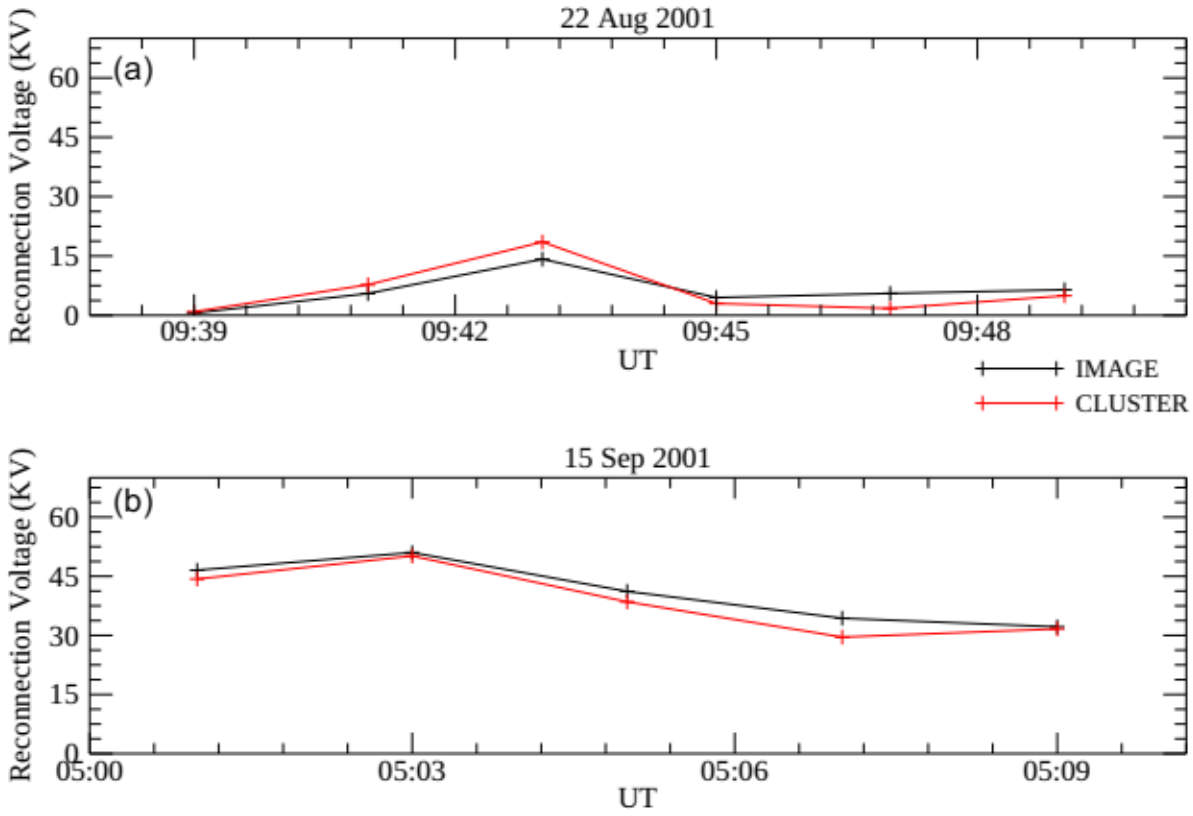

Figure 13. Comparison of the reconnection voltages of the IMAGE and the Cluster satellites on (*a*) 22 August 2001, and (*b*) 15 September 2001. Both cases produce the same conclusion that both methods closely agree.

Another, more complicated case was successfully analysed when Cluster crossed the dayside reconnection site. This result was not published because of the complexity of the treatment it requires, which makes its conclusions more fragile. The result was, nevertheless, that there is also a good agreement between both methods concerning the dayside reconnection rate.

Our analysis of the energy input into the reconnecting magnetic structure revealed that only a fraction of that energy, on the order of 40% and ranging between 20 and 85% during the restricted studied intervals, is dissipated in the substorm aurora. This highlights that the energy transfer between the magnetotail and the auroral ionosphere is not immediate, and that the energy released by the tail is distributed between the different parts of the system. We anticipate over the next section to mention that no obvious plasmaspheric signature was observed when we analysed strong substorms. So that the partition of energy between the elements of the system does not produce a direct, obvious disturbance of the cold, trapped population. It was already known before that the trapped populations are not much sensitive to the substorm cycle. We found that even when the reconnection rate can be estimated, no clear signature is found. We speculate that the time scale of the substorm expansion phase, about half an hour, is too different from the time scale of the drift motion of trapped particles (several hours) for a direct influence to be seed. Moreover, the trapped populations and the reconnection process are phenomena belonging to different parts of the magnetotail, along field lines having a very different topology. It remains that the trapped population is often considered as an important source of particles feeding the aurora. The absence of apparent correlation between the flux closure rate and the plasmasphere density over short time scales does however not preclude from

a part of that energy to be ceased to the trapped population over long time scales. From a thermodynamic standpoint, energy stored in the system is expected to distribute among its parts over time. Generation of waves dissipating a part of the plasma energy is surely a mechanism to be considered as well.

The magnetic flux opening and closure cycle is at the heart of the dynamic coupling between the Earth magnetosphere and the solar wind. Having a method that allows for its monitoring using imaging and radar observation of the polar aurora is an important asset for any study of the auroral and magnetospheric phenomena, especially considering that it can be achieved using observational methods and techniques that are well mastered. We therefore consider that such method should be improved and further analysed in order to give support to future space missions dedicated to the field.

4.5 Magnetic reconnection and ionospheric signatures during major storms.

Geomagnetic storms occur under very intense forcing by the solar wind, especially when the solar wind speed is large. They differ from substorms by the magnitude of the magnetospheric response they induce, which extends to the scale of the whole planet, including the radiation belts and ring current. Therefore, they induce a magnetic disturbance down to the equatorial response, synthesized by the Dst index which can be viewed as a proxy evaluating the energy of the ring current. The L-shell location of the plasmapause (L_{pp}) was estimated from the IMAGE-EUV observation of the plasmasphere during two major storm intervals. Figure 14 illustrates the retrieval of the plasmapause location for one EUV image. The reconnection rates and open magnetic flux were estimated from the IMAGE-SI12 observation of the proton aurora, combined with the SuperDARN radar measurement of the ionospheric convection. The location of the Heppner-Maynard boundary (HMB) was also determined from the SuperDARN observation.

Our analysis shows that the Dst index, and therefore the energy of the ring current, correlates with the open magnetic flux, but not with the reconnection rate. This suggests that the energy released by flux closure is not directly ceased to the ring current particles at storm time. However, if we consider that the open magnetic flux is an indicator of the energy stored in the tail, then we speculate that the correlation can be interpreted in terms of a partition of the energy between the different parts of the system, as one would expect from the principles of thermodynamics. As the cycle of opening and closure of magnetic flux is driven by the solar wind properties, some degree of correlation was also found with the solar wind parameters. For example, a dependence of Dst is found with the solar wind velocity, but this is not something new. Figure 15 shows the Dst index recorded during both storm intervals studied for the MOMA project, that occurred in August 2000 and April 2001. Both present two clear storm signatures, with the Dst index decreasing to very low values.

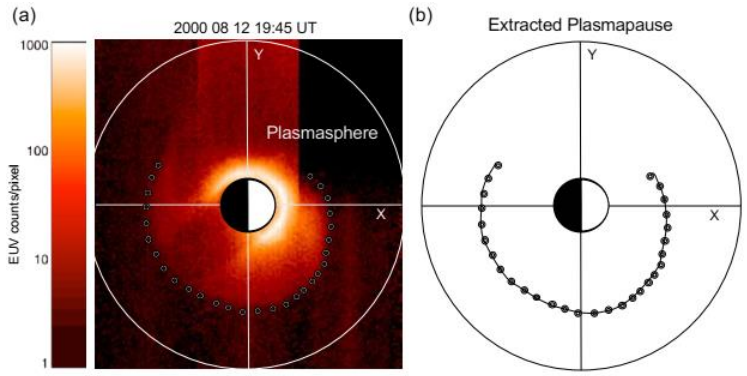

Figure 14. Extraction of the plasmapause curve from the IMAGE EUV plasmaspheric observations of one of the studied storm days; 12 August 2000, 19:45 UT. (a) EUV image, mapped to the magnetic equator (Earth at centre and Sun to the right). Filled circles are manually extracted ('click') points along the plasmapause. (b) Fourier expansion of the click points (circles) is plotted as the solid curve (Inspired from Goldstein et al., 2004).

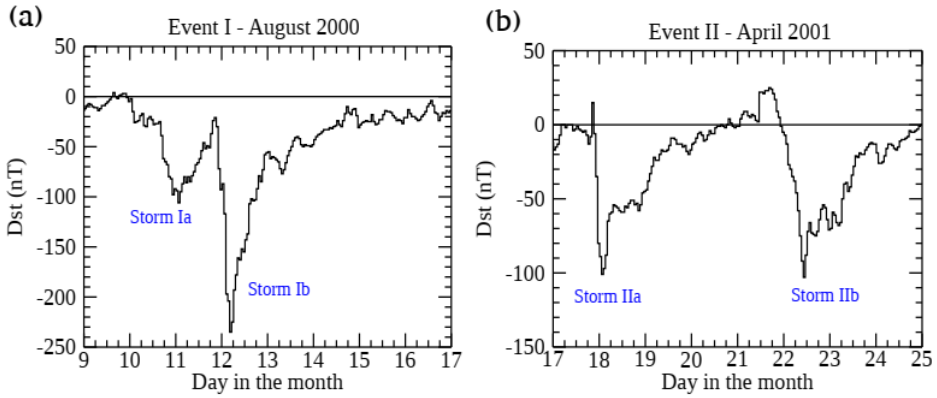

Figure 15. Dst index as a function of time for the major storms occurring in (*a*) August 2000 (Event I) and (*b*) April 2001 (Event II). Two "storm intervals": the two activations during the first interval (August 2000) being treated throughout as one event (Storms Ia and Ib), while the second interval (April 2001) contains two clearly separated storms (Storms IIa and IIb).

As two storms were recorded during both intervals, a correlation study based on both full periods of time mixes periods of high and low activity. The correlations that were found are stronger when restricting the analysis to the most active portions of the interval, as shown below in Table 2. Symbols V_{op} ,V_{net} and V_{cl} denote the opening, net and closure reconnection voltages, Φ is the open magnetic flux, V_{SW}, Dens, P_{Dyn}, $|B|$, B_x, B_y, B_z, and E_y are the solar wind velocity, density, dynamic pressure, magnetic magnitude and x, y, z components and y component of the electric field. A clear correlation is found between Dst and Lpp, indicating that, when the ring current is increased, the plasmapause is also retracted Earthward. This suggests that the convection electric field is increased at times of increased ring current energy. This conception is however more relevant at steady state, while geomagnetic storms are very dynamic. Similar results are obtained during the September 2001 interval.

	Dst	V_{op}	V_{net}	V_{cl}	Φ	L_{pp}
Dst	-	-0.231	0.107	0.349	-0.666	0.892
	-	-0.197	0.033	0.192	-0.665	-0.869
V_{sw}	-0.738	0.091	-0.065	-0.171	-0.083	-0.435
	-0.651	0.076	-0.002	-0.059	0.152	-0.606
Dens	-0.246	0.034	-0.037	-0.082	-0.330	0.034
	-0.224	0.080	0.005	-0.053	-0.130	-0.177
P_{Dyn}	-0.548	0.083	-0.070	-0.171	-0.262	-0.225
	-0.411	0.097	-0.015	-0.093	-0.032	-0.380
|B|	-0.721	0.220	-0.108	-0.342	0.340	-0.509
	-0.809	0.191	-0.028	-0.185	0.429	-0.619
B_x	-0.219	0.298	0.147	-0.041	0.322	-0.085
	0.021	0.137	0.080	0.009	0.041	-0.057
B_y	-0.438	0.099	-0.226	-0.408	0.349	-0.301
	-0.562	0.095	-0.074	-0.177	0.487	-0.323
B_z	0.453	-0.394	-0.054	0.255	-0.759	0.248
	0.438	-0.228	-0.040	0.118	-0.716	-0.187
Φ	-0.666	0.269	-0.044	-0.291	-	-0.708
	-0.665	0.170	-0.095	-0.263	-	-0.539
E_y	-0.495	0.405	0.056	-0.265	0.751	0.119
	-0.450	0.246	0.038	-0.131	0.712	0.067

Table 2. Pearson correlation coefficient computed between different solar wind parameters and the Dst index, reconnection voltages, open magnetic flux (Φ), and average plasmapause radial distance Lpp for the storm of August 2000. In black are the values deduced during the main phase of the storm and in purple are the values deduced during the entire interval between the 9th and 17th of August 2000.

Table 1 shows that larger correlations are found between the parameters describing the system during the most active sub-intervals. This was also found when studying the flux of high energy electrons measured by the GOES 8, 10 and 11 satellites at geosynchronous altitude. This orbit places the spacecraft somewhat outside of the plasmasphere for most of the time. However, the entrapment of very high energy particles is not limited to the plasmasphere. High energy particle orbits are rather limited by the Alfvén layers, that account for the gradient and curvature drift, rather than the corotation electric field. Those Alfvén layers can extend beyond the plasmapause, depending on the particle energy and the intensity of the convection electric field. It is therefore not really surprising to find a correlation between the GOES particle flux measurement and the Dst index under active storm conditions, as was found for both events studied for the MOMA project.

The HMB colatitude was also found to correlate with L_{pp} at storm time, with Pearson correlation coefficients ranging between -071 and -087 for the different active subintervals of the study. This highlights the consistent evolution of the trapped population retracting Earthward when the convection electric field increases, the convection zone then extending to field lines having their ionospheric footprint at lower latitude. Along similar lines, the auroral electrojet indices, that synthesize the magnetic response induced at high latitude by the electric current flowing in the auroral zone, were also found to correlate with L_{pp}. At storm time, the whole planetary system is disturbed, and the dissipation of the energy present in the system is reflected in all the mechanisms at play, at all latitudes.

The correlation between the storm time indicators and the open magnetic flux is very specific of the study conducted for the MOMA project. It stands along the line of the results of section 4.2 regarding

energy distribution and dissipation in the system, as the open magnetic flux is a quantitative indicator of the energy stored in the magnetic field while the Dst index is an indicator of the energy stored in the ring current. Future studies aiming at understanding how energy circulates and is distributed in the magnetosphere can therefore benefit from methods used to estimate the open magnetic flux and the reconnection rate, not only at storm time.

4.6 : Polarization of auroral lights

We had the opportunity during the last observation campaign in March 2020 to use another instrumental prototype instrument developed in-house, called the Polar Lights Imaging Polarimeter (PLIP). This a low budget set-up, with two identical cameras (Canon 6D) coupled with also two identical 24 mm lenses opened at F/2.8, fixed on a tripod. Only the Q component of the linear polarization is traceable here, using two fixed polarizers oriented at 0° and 90°. The camera are GPS-sync so that the exposure time of each camera are correctly synchronized to measure simultaneously the +Q and –Q components. We considered 20 second intervals between each frame, with a 15s exposure time, allowing a 5 seconds reset. We were able to observe for almost 2h, during clear-sky conditions, with some intense auroral activity. To select the auroral emission spectral lines, we did used some green and red commercial large bandpass filters. However, after characterizing these filters in the optical lab at BIRA-IASB, we discovered that a substantial part of the infrared spectrum (700 – 1100 nm) was not efficiently filtered out, which could interfere with our results.

Later on, we have therefore developed a new improved version of the instrument, PLIP 2.0, with two sensitive low-noise level CMOS cameras with large FOV (~30° × 25°) equipped with fixed polarizers oriented at 0° and 90° allowing to measure the Q Stokes parameter on a large portion of the sky. Narrow interference filters ($\Delta\lambda$~10 nm) with central wavelengths at 427.8, 557.7 and 630.0 nm can be inserted in the optical path using filter wheels. The filters have been designed in order to make sure that the wavelength of interest still falls within the band even for light rays with a large angle to the optical axis. The PLIP 2.0 instrument has been calibrated at the Laboratoire d'Optique Atmosphérique (LOA) in Lille with a collimated white lamp with controlled level of polarization. The response of both optical systems being different, these calibrations allowed us to determine a calibration linear fit in order to correct for the camera responses. We already performed some tests at the radio-astronomical site of Humain, looking at the Rayleigh polarization of the daylight at Sunset or of the night-sky due to Rayleigh scattering of the moonlight. At Sunset, with known coordinates, the Rayleigh sky model as depicted in Figure 16 provides the DoLp as well as the Q maps.

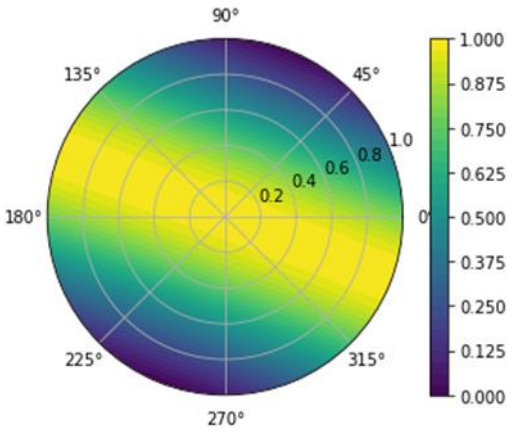

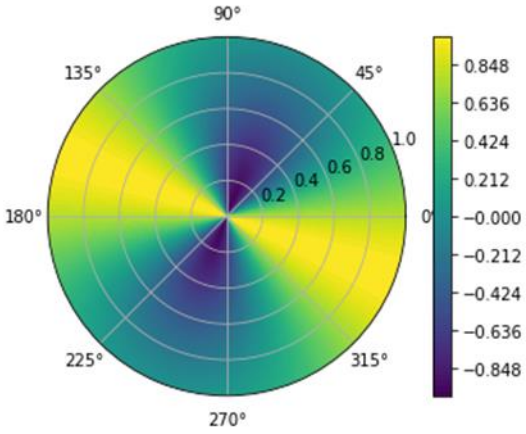

Figure 16: Rayleigh sky model providing DoLP (left) and Q values (right) for the Sunset at Humain.

Some tests were then performed with the PLIP 2.0 instrument, for different observations directions, one close to the maximum DoLP band, and one at the antisolar diection in order to look for almost no light polarization. Some results are displayed in Figure 17, with the red filter for both directions, after correction using the linear fit from the calibration performed in Lille. The results are pretty consistent with the theory, and the discrepancies with the Rayleigh sky model are likely due to the aerosol content which tends to depolarize the light, which was not considered here.

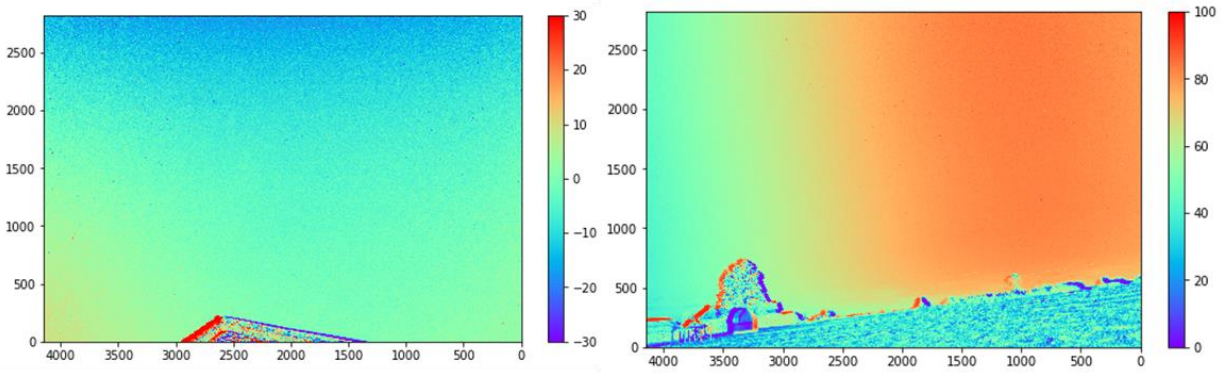

Figure 17: Q values for the red filter using PLIP 2.0, looking at the antisolar direction (left) and at 310° azimuth (right)

Observations of auroral light polarizations with PLIP 2.0 will be carried out in December 2021 at the Public Observatory of the University of Tromsø, located in Skibotn, Norway. A full version of the instrument using 4 channels (CMOS cameras, filter wheels and fixed polarizing filters) will be ready for another campaign in Skibotn in March 2022, allowing to measure the full DoLP (and therefore AoLP).

References

- Barrett, J. L., and P. B. Hays (1976), Spatial distribution of energy deposited in nitrogen by electrons, J. Chem. Phys., 64, 743–750, doi:10.1063/1.432221.
- Bertaux et al., Nature, 435, 790-794, doi:10.1038/nature03603, 2005
- Bhardwaj & Gladstone, Rev. Geophys., 38, 295-354, doi: 10.1029/1998RG000046, 2000.
- Bommier et al., The theoretical impact polarization of the O I 6300 Å red line of earth aurorae, Ann. Geophys., 29, 71-79, doi: 10.5194/angeo-29-71-2011, 2011
- Borovsky, J. Geophys. Res., 98, 6101–6138, doi:10.1029/92JA02242, 1993
- Bosse, L. et al, On the nightglow polarization for space weather exploration, JSWSC, Vol 10, id.35, 2020
- Bosse, L. et al, The auroral emissions polarization, a tracer of the E region ionospheric currents, submitted to JSWSC, 2021a
- Bosse, L. et al, Night light polarization: modeling and observations of light pollution in the presence of aerosols and background skylight or airglow, submitted to JSWSC, 2021b
- Coumans et al. , Ann. Geophys., (22), 1595-1611, 2004
- Echim et al., Coupling between LLBL and post-noon/evening discrete aurora through field-aligned currents: a quasi-stationary kinetic model, Ann. Geophys., 25,.317-330, doi:10.5194/angeo-25-317-2007 , 2007.
- Echim et al., Ionospheric feedback effects on the quasi-stationary coupling between LLBL and postnoon/evening discrete auroral arcs, Ann. Geophys., 26, 913-928, 2008.
- Echim et al., A magnetospheric generator driving ion and electron acceleration and electric currents in a discrete auroral arc observed by Cluster and DMSP, Geophys. Res. Lett., 36, doi: 10.1029/2009GL038343, 2009
- Echim, M. et al, A Method to Estimate the Physical Properties of Magnetospheric Generators from Observations of Quiet Discrete Auroral Arcs, JGR: : Space Physics, Vol 124, Issue 12, 2019
- Frey et al., J. Geophys. Res., 115, A10209, doi:10.1029/2010JA015537, 2010
- Gérard J.C., B. Hubert, D.V. Bisikalo and V.I. Shematovich, A model of the Lyman-alpha line profile in the proton aurora, J. Geophys. Res., 105, 15795-15805, 2000
- Gunell et al., Ann. Geophys., 31, 1227-1240, doi:10.5194/angeo-31-1227-2013, 2013
- Gurnett, J. Geophys. Res., 79, 4227-4238, 1974
- Hallinan et al., Nature, 523, 568-571, doi : 10.1038/nature14619, 2015
- Hubert B., J.C. Gérard, D.S. Evans, M. Meurant, S.B. Mende, H.U. Frey and T.J. Immel, Total electron and proton energy input during auroral substorms: remote sensing with IMAGE-FUV, J. Geophys. Res. (Space Physics), 107, doi: 10.1029/2001JA009229, 2002.
- Hubert, B. , S.E. Milan , A. Grocott, S. W. H. Cowley, and J.-C. Gérard, Dayside and nightside reconnection rates inferred from IMAGE-FUV and SuperDARN data, J. Geophys. Res., 111, A03217, doi:10.1029/2005JA011140, 2006
- Janhunen, P., Reconstruction of electron precipitation characteristics from a set of multiwavelength digital all-sky auroral imagesGeophys. Res., 106, 18505–18516, doi:10.1029/2000JA000263, 2001
- Kivelson, M., Kivelson, M., & Russell, C. (1995). Introduction to space physics. Cambridge University Press.
- Louarn & Le Quéau, P&SS, 44, 199-210, doi:10.1016/0032-0633(95)00121-2, 1996a

- Louarn & Le Quéau, P&SS, 44, 211-224, doi:10.1016/0032-0633(95)00122-0, 1996b
- Mende, S.B., H. Heetderks, H.U. Frey, M. Lampton, S.P. Geller, S. Habraken, E. Renotte, C. Jamar, P. Rochus, J. Spann, S.A. Fuselier, J.C. Gérard, G.R. Gladstone, S. Murphree, and L. Cogger, Far ultraviolet imaging from the IMAGE spacecraft: 1. System design, Space Sci. Rev., 91, 243, 2000a.
- Mende, S.B., H. Heetderks, H.U. Frey, J.M. Stock, M. Lampton, S. Geller, R. Abiad, O. Siegmund, S. Habraken, E. Renotte, C. Jamar, P. Rochus, J.C. Gérard, R. Sigler, and H. Lauche, Far ultraviolet imaging from the IMAGE spacecraft : 3. Spectral imaging of Lyman alpha and OI 135.6 nm, Space Sci. Rev., 91, 287, 2000b.
- Milan et al., J. Geophys. Res., 112, A01209, doi:10.1029/2006JA011642, 2007
- Mutel et al., Geophys. Res. Lett., 35, CiteID L07104, doi:10.1029/2008GL033377, 2008
- Nichols & Milan, MNRAS, 461, 2353-2366, doi: 10.1093/mnras/stw1430, 2016
- Partamies, N., P. Janhunen, K. Kauristie, S. Mäkinen, and T. Sergienko, Testing an inversion method for estimating electron energy fluxes from all-sky camera images, Ann. Geophys., 22, 1961–1971, 2004, doi:10.5194/angeo-22-1961-2004.
- Sergienko & Ivanov, A new approach to calculate the excitation of atmospheric gases by auroral electron impact, Ann. Geophys., 11, 717–727, 1993
- Simon Wedlund et al., Estimating energy spectra of electron precipitation above auroral arcs from ground-based observations with radar and optics, J. Geophys. Res., 118, 3672-3691, doi:10.1002/jgra.50347, 2013.
- Stallard et al., Nature, 456, 214-217, doi: 10.1038/nature07440, 2008
- Vaivads, A. et al, What high altitude observations tell us about the auroral acceleration: A Cluster/DMSP conjunction, Geophys. Res. Lett., 30, 2003, doi:10.1029/2002GL016006

5. DISSEMINATION AND VALORISATION

Below is the list of communications given at various international conferences

- Cessateur, G. ; Lamy, H. ; Simon Wedlund, C. ; Gustavsson, B. ; Gronoff, G., Fluxes of precipitating magnetospheric electrons from ground-based optical observations of auroral arcs, AGU Fall Meeting 2018, abstract #P21C-3372
- Gronoff, G. ; Lamy, H. ; Cessateur, G. ; Simon Wedlund, C. ; Lovato, K. ; Gustavsson, B., Multi-wavelength modeling of an auroral arc observed with EISCAT and ALIS using the Aeroplanets model, AGU Fall Meeting 2018, abstract #P21C-3373
- Lamy, H. ; Echim, M. ; Cessateur, G. ; Simon Wedlund, C. ; Gustavsson, B. ; Maggiolo, R. ; Gunell, H. ; Darrouzet, F. ; De Keyser, J., From discrete auroral arcs to the magnetospheric generator: numerical model and case study, AGU Fall Meeting 2017, abstract #SM31B-2625
- Matar J., B. Hubert, S. Cowley, S. E. Milan, Z. Yao, R. Guo, J. Goldstein, B. R. Sandel and C. A. Gurgiolo (2020). The Plasmasphere During Geomagnetic Storms, AGU Fall Meeting 2020, San Fransisco, USA, abstract #SM040-0001.
- Matar J., B. Hubert, S. Cowley, S. E. Milan, Z. Yao, R. Guo, J. Goldstein, and B. R. Sandel (2020), The Plasmasphere During Major Geomagnetic Storms: Analysis Of Trapped Particles In The Outer Radiation Belt EGU General Assembly 2020, Online, 4–8 May 2020, EGU2020-265, https://doi.org/10.5194/egusphere-egu2020-265, 2019
- Matar J., B. Hubert, Z. Yao (2019), Trapped Population Response During Geomagnetic Auroral Super Storms, 16th European Space Weather Week, ESWW 2019, Liège, Belgium, 2019
- Matar J., B. Hubert, Z. Yao, R. Guo, S. E. Milan, S. W. H. Cowley (2018), Study Of The Energy Budget During Isolated Auroral Substorms, AGU Fall Meeting 2018, Washington D.C., USA, 2018

The presentations given during the MOMA kick-off meeting and annual meetings can be found on the MOMA website : https://moma.aeronomie.be/

6. PUBLICATIONS

- Barthélemy, M. ; Lamy, H. ; Vialatte, A. ; Johnsen, M.G. ; Cessateur, G. ; Zaourar, N., Measurement of the polarisation in the auroral N2+ 427.8 nm band, Journal of Space Weather and Space Climate, Volume 9, https://doi.org/10.1051/swsc/2019024
- Borovsky, J. E.; Birn, J.; Echim, M. M.; Fujita, S.; Lysak, R. L.; Knudsen, D. J.; Marghitu, O.; Otto, A.; Watanabe, T.-H.; Tanaka, T., Quiescent Discrete Auroral Arcs: A Review of Magnetospheric Generator Mechanisms, Space Science Reviews, Volume 216, 2020
- Dekemper E., Vanhamel J., Kastelik J.-C., Pereira N., Bolsée D., Cessateur G., Lamy H., Fussen D., New AOTF-based instrumental concepts for atmospheric science, Proc. of SPIE Vol. 11210, 2020.
- Echim, M. M. ; Lamy, H. ; De Keyser, J. ; Maggiolo, R. ; Gunell, H. ; Simon Wedlund, C. L, A Method to Estimate the Physical Properties of Magnetospheric Generators From Observations of Quiet Discrete Auroral Arcs, J. Geophys. Res., 124, Issue 12, 10283-10293, 2019. https://doi.org/10.1029/2019JA026969
- Matar, J., Hubert, B., Yao, Z., Guo, R., Cowley, S. W. H., Milan, S. E., & Gurgiolo, C. (2020). Concurrent observations of magnetic reconnection from Cluster, IMAGE and SuperDARN: A comparison of reconnection rates and energy conversion. *J. Geophys. Res*, 125, e2019JA027264. https://doi.org/10.1029/2019JA027264
- Matar J., S.W.H. Cowley, S. E. Milan, Z.Yao, R. Guo, B. Sandel, J. Goldstein, C. Gurgiolo, and B.Hubert, (2021), The Plasmasphere During Major Geomagnetic Storms: Relation With Auroral Activity And Other Parameters, *J. Geophys. Res.*, submitted
- Matar J., Effect Of Magnetic Reconnection Over The Earth's Space Environment, a thesis.

7. ACKNOWLEDGEMENTS

We would like to thank the members of the follow-up committee for their active participation during this MOMA project and in particular their presence at the annual MOMA meeting.

- Dr. Mathieu Barthélemy (IPAG, France)
- Dr. Noora Partamies (UNIS, Norway)
- Dr. Jérôme Loicq (CSL, Belgium)

We would also like to thank all the invited participants who kindly contributed to the annual MOMA meetings. Their names and presentations are listed on the MOMA website: https://moma.aeronomie.be/

The PLIP instrument was built using funding from the Solar-Terrestrial Center of Excellence (STCE).